

# DESIGN CONSIDERATIONS OF A PRESSURE DRIVEN MORPHING WING STRUCTURE

**Srinivas Vasista and Liyong Tong**

**University of Sydney, Sydney, NSW 2006, Australia**

*srinivas.vasista@sydney.edu.au; liyong.tong@sydney.edu.au*

**Keywords:** *morphing, compliant mechanism, topology optimization*

## Abstract

*A compliant cellular structure driven by pneumatic pressure was designed in this work. The cell shape was determined via topology optimization and the optimum shape was found to consist of two arches which open and elongate to provide bending or extension. Converting these shapes into a thin walled structure and after a parametric study, the best cell parameter values (depth and length of the top arch and vertical-lower arch connection point) were determined based on deflection, stiffness and stress considerations. A bimorph-type morphing trailing edge for a NACA 0012 aerofoil was mapped from this thin-walled compliant cellular structure. Finite element analysis showed feasibility of the concept and testing of a preliminary prototype specimen further demonstrated the working principle. The specimen was fabricated from glass fiber reinforced plastic and at 14 kPa pressure a maximum downward tip deflection of 13.9° was observed.*

## 1 Introduction

It is well documented that the implementation of morphing structures in aircraft may lead to improved aircraft performance [1-3]. One of the emerging trends in morphing wing research is the use of a coupled fluid pressure - cellular structure system. In this type of system, analogous to the motion of plants in nature, the cell structural material and fluid pressure combine to provide both shape change and stiffness functions in an integrated manner, this being a key challenge in morphing wing design. An example of this type of system is a nastic

structure/actuator which consists of arrays of microhydraulic cells embedded in a polymeric plate [4]. Increasing the pressure in the cells results in cell deformation and accumulating these deformations over the many cells results in macroscopic shape change. Other technologies include pressurized flexible matrix composites (FMCs) [5, 6] and fluidic flexible composites (F<sup>2</sup>MCs) [7]. Furthermore, the "Pressure Adaptive Honeycomb" concept was recently developed and applied to a morphing wing flap [8, 9]. This concept featured a honeycomb structure with air-tight bladders contained within the hexagonal honeycomb cells. The overall stiffness of the structure could be varied by varying the cell differential pressure. With the addition of restoring forces, the variation in stiffness enabled the structure to deform as a function of the cell differential pressure [8].

In another approach [10], it was shown that topology optimization methods (SIMP and MIST) can be used to design the cell shape. Various cellular architectures were considered for unimorph, bimorph and extension morphing. Various cell shapes were analyzed for an aerofoil trailing edge section in [11].

In this work, we develop this topologically optimized morphing concept further and aim to determine ways of implementing this concept in a three-dimensional wing structure. An overview of the topology optimization problem is presented first along with a 2D resultant cell design. Some considerations on how to implement these optimization results into a real wing structure are then discussed, leading into the description of the method and results of a parametric study on the optimized cell shape. The three-dimensional structure is then applied

to a morphing wing trailing edge and the ensuing finite element analysis and experimental testing results are discussed.

## 2 Topology Optimization Using MIST

The Moving Iso-Surface Threshold (MIST) topology optimization method [12] was used to obtain a two-dimensional planar cell design which is driven by fluid pressure. The problem formulation was that of a compliant mechanism as shown in Eqn 1 using incompressible elements and the mixed u/P finite element formulation [13, 14]. The reader is referred to [10] for details on the implementation and validity of the method.

$$\begin{aligned}
 \max: u_{out} = \min: -u_{out} &= - \int_{\Omega} \boldsymbol{\sigma}^{(2)T} \boldsymbol{\varepsilon}^{(1)} d\Omega \\
 \text{s. t. : } \mathbf{K}\mathbf{u} + \mathbf{C}\mathbf{p} &= \mathbf{f} \\
 \mathbf{C}^T \mathbf{u} - \mathbf{D}\mathbf{p} &= \mathbf{0} \\
 \int_{\Omega} x d\Omega / \int_{\Omega} d\Omega &\leq f_{solid} \\
 0 < x &\leq 1
 \end{aligned} \tag{1}$$

In this paper the optimization case was a cell designed for bending.  $60 \times 60$  elements were used along with a material volume fraction of 0.35, solid bulk and shear moduli of 10 and  $1/2.6$  respectively, fluid bulk and shear moduli of 10 and 0.001 respectively and a penalization factor of 3 (refer to [13] or [10] for material interpolation schemes). A move limit of 0.1, an output spring stiffness of 0.5 and a density filter size of 1.5 were also used. The optimization setup and results are shown in Fig. 1. The cell shape is fairly intuitive: the main lower arch opens up as the cell is pressurized, facilitated by the smaller upper arch elongating. With this elongation the top corner points move outwards relative to the bottom corner points, thus resulting in bending.

## 3 Overview of the Application of the Optimization Result to Wing Structure

Multicell designs based on the result in Fig. 1 were presented in [10] and [11] for planar rib-type structures. The architecture types were

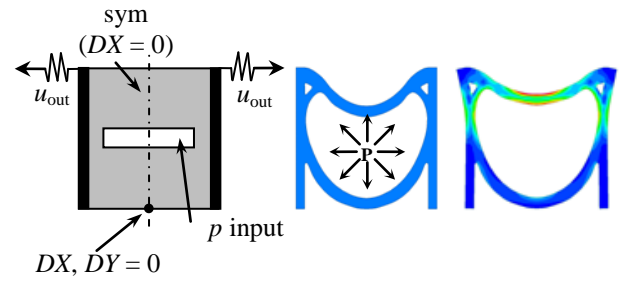


**Fig. 1** Design domain, optimization result and deformation profile with von Mises stress contours.

series connections for unimorph morphing and bimorph morphing. However, it is more practical to convert these cellular networks into a three-dimensional structure as opposed to two-dimensional planar as large spanwise bending moments/torsion loads need to be supported. Furthermore, it is difficult to apply pressure on a thin edge and as pressure is omnidirectional (i.e. three-dimensional), an efficient three-dimensional design is required. One method of converting the optimization result in the three-dimensional design is to extrude the cell design in the spanwise direction. Assuming a constant (untapered) cross section along the spanwise direction, the kinematics of the deformation remain similar to that of the two-dimensional case. However, this extrusion results in a thick-walled, heavy structure requiring either a large input pressure or a low modulus material to enable morphing. This morphing design can be converted into a lightweight thin-walled high modulus structure (as in traditional aircraft structures) by extruding the centrelines of the cell topology. It should be noted that the thickness of arches become smaller if lower values of the volume fraction constraint are used in the optimization process, though very low volume fraction constraints (e.g. in the order of

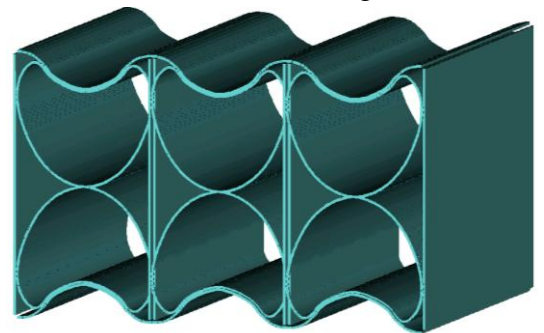


**Fig. 2** Conceptual design of thin walled extruded topology optimization result.

0.05) should be avoided for numerical reasons. A diagram of this concept is shown in Fig. 2. This type of structure can be fabricated with metallic or composite materials via such methods as molding and lay-ups, hydroforming and/or additive layer manufacturing. With this new thin-walled structure, the cell geometry needs to be defined in terms of points, curves and lines. Also, modifying the design in such a way allows for the effects of geometric parameters to be analyzed, as is described in the next section.

#### 4 Parametric Study

##### 4.1 Cell Geometry Definition and Parametric Study Method

A parametric study was conducted to determine the effect of and to "tweak" the geometry to obtain better performance. This study involved conducting finite element analysis for a range of cell geometries. The cell shape cross section (half, using symmetry) was characterized by six points, two splines and a straight line. This was further simplified into three parameters as shown in Fig. 3: the depth  $D$  of the top arch, the length  $L$  of the top arch and the vertical distance  $M$  from the top corner to the point of tangency between the lower arch and the vertical line. In order to define the geometry, constraints were applied to the splines and points. Horizontal tangency was enforced on the splines at points 1, 3 and 5, points 1, 2 and 3 were collinear, point 2 was the inflexion point of spline 1 and spline 2 was tangent to the vertical line at point 4. Furthermore, the end slope of spline 2 at point 2 was allowed to be adjusted so as to obtain a maximum radius of curvature in spline 2 though a lower limit of  $0^\circ$  (horizontal) was enforced. This is indicated by the curved arrow.

Fig. 4 shows the structural model used in the parametric study. 2D beam elements were used to simplify the analysis. Two load cases were considered separately in the parametric study to assess the shape-change and load-capability (stiffness) performance. A uniform pressure was applied on the inside edge of the central region for load case 1 and a linearly distributed load in the x-direction was applied to

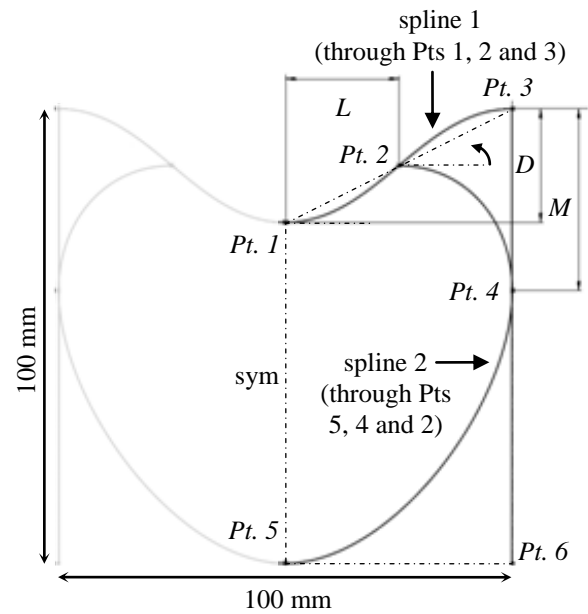
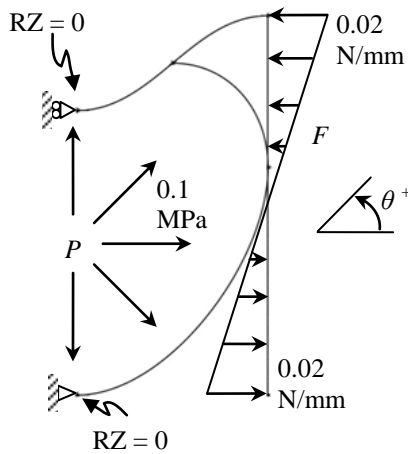


Fig. 3 Thin-walled cell geometry and parameters.

the right vertical edge for load case 2. It should be noted the load in the force case causes the cell to bend in the opposite direction to that of the pressure in load case 1. The structure's shape-change performance was obtained from the pressure load case and the structure's unpressurized stiffness performance was obtained from the force load case by measuring the average rotation of the right edge for both cases.

The implementation of the study is described as follows: the cell geometry files were created using a CAD program. These files were then read in MATLAB and the finite element analysis input file was solved using ANSYS APDL (executed within MATLAB). The ANSYS results were then read into MATLAB and graphed. It should be noted that after the geometry files were created, the pre-processing, solution and post-processing stages conducted in MATLAB and ANSYS were automated.

The full cell dimensioned  $100 \times 100$  mm.  $D$  ranged from 10 to 40 mm,  $M$  ranged from 30 to 50 mm and  $L$  ranged from 20 to 35 mm. The increment for all three parameters was 5 mm and in total 140 different cell geometries were analyzed. A Young's Modulus of 70 GPa and Poisson's ratio of 0.3 were used for beam

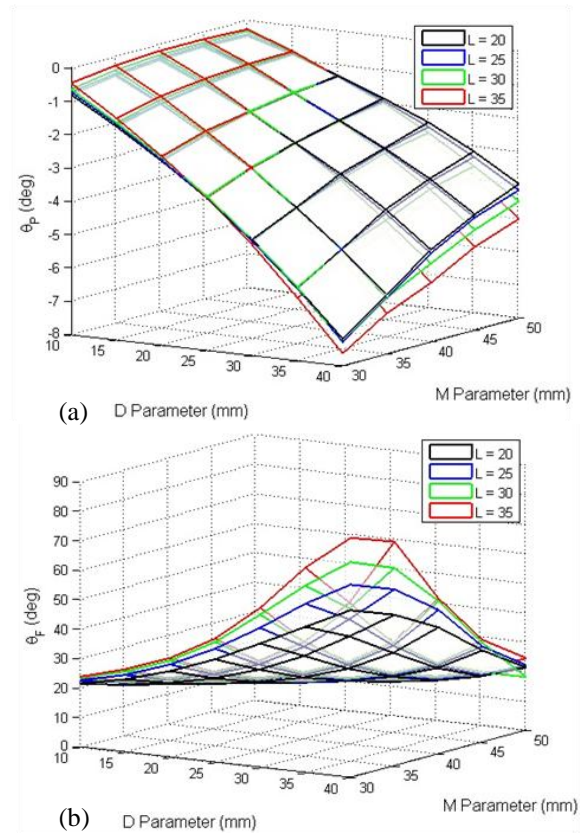


**Fig. 4** Half cell structural model showing pressure  $P$  and force  $F$  load cases.

elements for splines 1 and 2, representative of an aircraft grade material. The beam elements on the vertical line were assigned a large Young's Modulus (1,000 GPa) to simulate a rigid material. The beam depth (into the page) was 1 mm for all beam elements. The thickness of all beams was 0.5 mm excluding those on spline 1 between Pts 2 and 3 for which the thickness was 1 mm. This double thickness was due to the topology optimization result featuring a thicker member in this region and also for manufacturing considerations. The magnitude of pressure was 0.1 MPa and the distributed load varied linearly between  $\pm 0.02$  N/mm to give resultant forces of 0.5 N in both the top and bottom halves of the vertical line. Geometric nonlinearities were included in the finite element analysis.

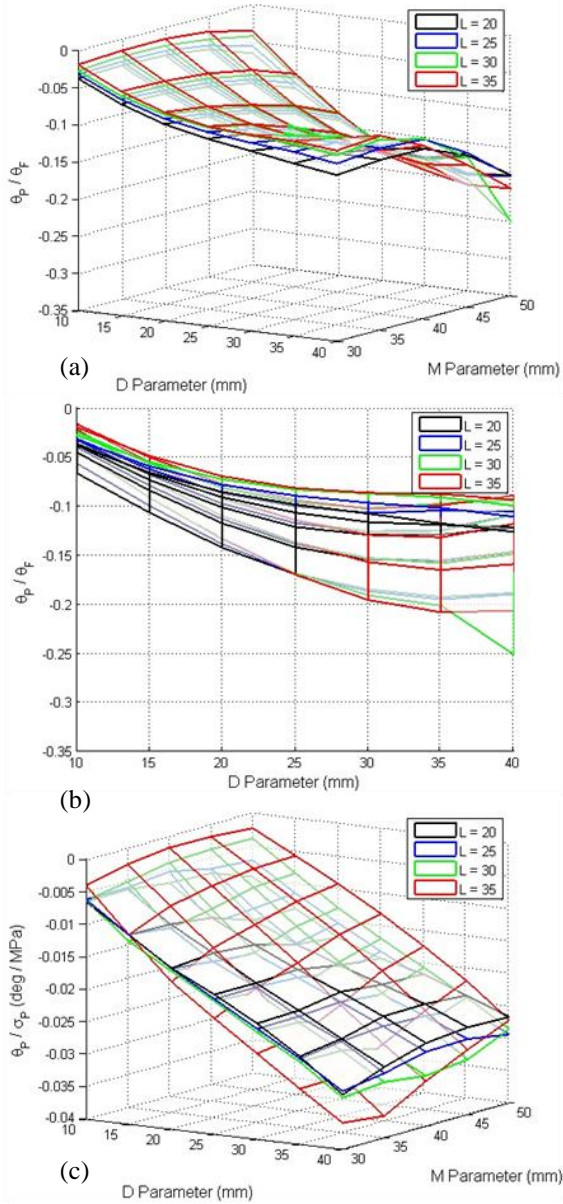
### 4.2 Results and Discussion

Fig. 5 (a) and (b) show the effect of the parameters on the average rotation on the right edge for the pressure and force cases respectively. The largest angular deflection for the pressure case  $\theta_P$  was  $-7.63^\circ$  at  $D = 40$ ,  $M = 30$ ,  $L = 35$ . From Fig. 5 (a) it is clear that  $D$  has the greatest effect on the rotation. This was expected as for larger depths the upper arch elongates more (horizontally) causing greater rotation (in the negative direction). It is also clear that increasing  $M$  results in reduced rotation as the "pivot" moves further down and



**Fig. 5** Average rotations on the right edge of the cell for (a) pressure and (b) force cases respectively,  $\theta_P$  and  $\theta_F$ . Positive rotation is anticlockwise.

reduces the downward rotation.  $L$  has a small effect on the rotation as the plot surfaces are reasonably close to each other, with increased rotation as  $L$  increases. The results and trends in Fig. 5 (b) are opposite to Fig. 5 (a). At the same design point as the maximum  $|\theta_P|$ , ( $D = 40$ ,  $M = 30$ ,  $L = 35$ ), the rotation due to force  $\theta_F$  was the highest with a value of  $81.07^\circ$ . Although undesirable, this trend was expected as flexibility and stiffness are contradictory goals. It should also be noted that the high value of  $\theta_F$  was due to low beam thicknesses and a relatively large distributed load. In addition, as this study was purely to assess the geometry of the cell shape, the effects of variables such as the magnitudes of the pressure and force, thickness, Young's Modulus and Poisson's ratio were not assessed. Alterations in these variables will result in changed final values of rotation. Rather than comparing single final values, we compare the trends of the effects of the parameters. Further measures were calculated to compare the combined shape-change and



**Fig. 6** Pressure-force rotation ratio (a) 3D view and (b) side view. (c) Rotation-maximum stress ratio for the pressure case.

stiffness performance of the different cell designs. These include the pressure-force rotation ratio  $\theta_p / \theta_F$  and pressure rotation-stress ratio  $\theta_p / \sigma_P$  where the location of the maxima of these values will be considered as the design point.

Fig. 6 shows the effect of parameters on the rotation ratio between pressure and force cases. In general higher  $M$  values give a better result and the  $L$  parameter has little effect on the rotation ratio. Fig. 6 (b) shows the same plot as

Fig. 6 (a) but from the side view (X-Z plane). There appears to be a stationary point or leveling-off of the curves between  $D = 30$  and 35 mm, with the exception of  $L = 30$  mm plot.

Fig. 6 (c) depicts the ratio of rotation to stress for the pressure case. The most notable trend is that higher values of  $D$  are desirable.

Based on this study the parameters chosen for the cell were:  $D = 30$ ,  $L = 30$ , and  $M = 45$ .

## 5 Aerofoil Design Case

### 5.1 Cell Geometry Mapping

The cell with geometry based on the parametric study was used in the design of a morphing trailing edge section. Ten cells were connected in a bimorph series arrangement comprising the region of 70 to 85 per cent chord length of a NACA 0012 aerofoil as shown in Fig. 7 (a) and (b). In order to conform to the aerofoil profile, the cell geometry was mapped from its initial square boundary to the region bounded by the aerofoil cell as shown in Fig. 7 (c) and using Eqns 2 and 3, where  $X_0^L$  is the x-coordinate of the left edge of the given cell in the  $X_0$  axis system. The aerofoil cell had a near-square aspect ratio as the cell width was made equal to average of the cell vertical side lengths. The length of this morphing region was 340 mm and a gap of 5 mm separated the cells. Stiff vertical inserts were placed in this gap. Fig. 8 depicts the design of the section in the wing structure with the cover skin absent.

$$X_2 = \left( \frac{W_2}{W_1} \right) X_1 \quad (2)$$

$$Y_2 = \left( \frac{Y_1}{H_1} \right) \frac{t}{0.2} c \left[ 0.2969 \sqrt{\left( \frac{X_2}{c} + \frac{X_0^L}{c} \right)} \dots \right. \\ \left. - 0.126 \left( \frac{X_2}{c} + \frac{X_0^L}{c} \right) - 0.3516 \left( \frac{X_2}{c} + \frac{X_0^L}{c} \right)^2 \dots \right. \\ \left. + 0.2843 \left( \frac{X_2}{c} + \frac{X_0^L}{c} \right)^3 - 0.1015 \left( \frac{X_2}{c} + \frac{X_0^L}{c} \right)^4 \right] \quad (3)$$

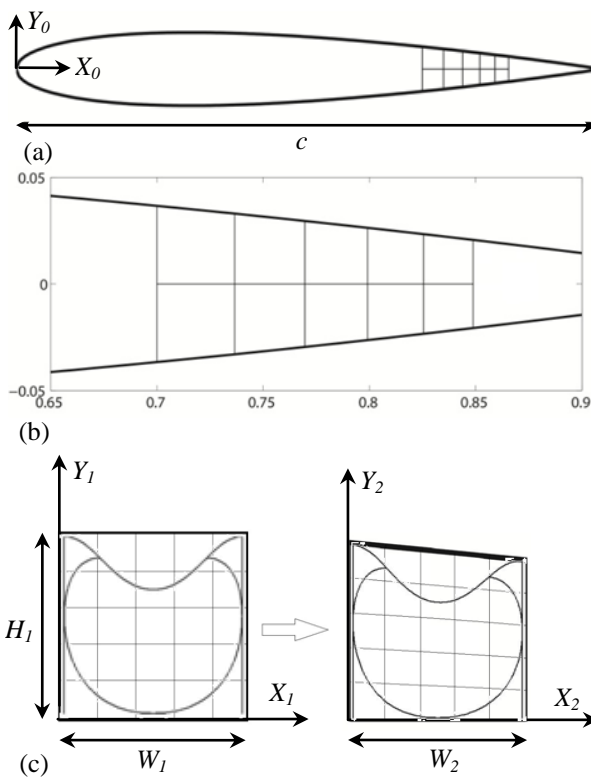


**Fig. 7** (a) Morphing trailing edge region of a NACA 0012 aerofoil. (b) Zoomed image of the morphing region. (c) Geometric mapping from master square cell to aerofoil cell.

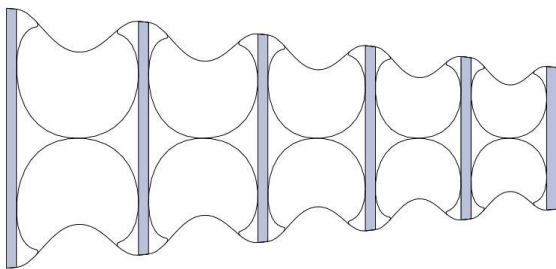


**Fig. 8** Morphing wing structure.

## 5.2 Finite Element Analysis of Wing Structure

The design in Fig. 8 was converted into a Strand7 finite element model as shown in Fig. 9.

Shell elements with 0.7 mm thickness were used for the thin arches and solid brick elements were used for the vertical supports between the cells. The material properties used were  $E = 45 \text{ GPa}$  and  $\nu = 0.3$ . The mesh topology was shared across the entire model: i.e. the shells and bricks were connected at common nodes and not via contact relations. The chordwise length of the structure was 340 mm and a spanwise length of 100 mm was used. The left most face and connector flanges at the top and bottom were fully fixed to model the fixed connection with the rear wing spar for example.

Three load cases were considered: i) a pressure-only case where the top five cells were pressurized to 340 kPa; ii) a force-only case where the top surfaces of the vertical members had a uniform pressure distribution amounting in total to  $50 \text{ kg}_f$  in the  $+Y$  direction; and iii) a combination of the above pressure and force load cases. Nonlinear geometrical effects were included in the finite element analysis.

For the case of the trailing edge flap/control surface, as a simple case we only consider the aerodynamic loads in the structural analysis and ignore other loads such as inertial loads. This is valid as flaps generally do not support wing payloads (engines, underwing pods, external fuel stores etc) and the weight of the flap structure itself is small to be ignored in this study. For this modeling we assume the rear spar is rigid and we aim to see how the morphing structure transfers the aerodynamic loads to the fixed rigid spar. This study was conducted to assess whether the current morphing design is feasible and it is not intended as a detailed analysis. The chord length of the whole morphing aerofoil (approximately 1.75 meters) is typical of that of light general aviation aircraft, such as the Cessna 152. For this type of aircraft, the cruise speed is in the order of 50 m/s.

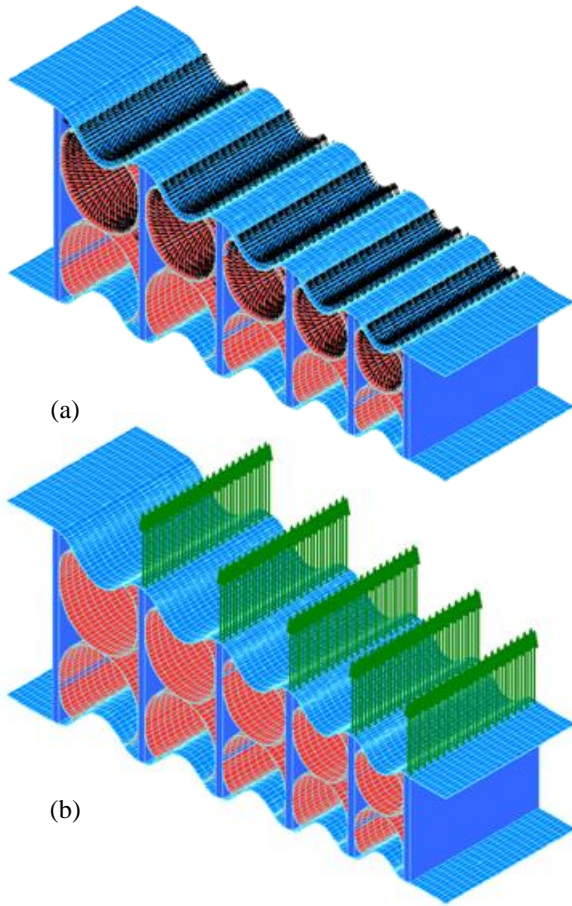


Fig. 9 (a) Pressure load case, top row of cells pressurized as shown by black arrows. (b) Force load case.

A modified NACA 0012 aerofoil was analyzed using XFOIL [15] to obtain the pressure distribution acting on the trailing edge portion. The aerofoil section was modified such that the flap/control surface was deployed to  $20^\circ$  and the region between  $0.7c$  and  $0.85c$  was smoothly contoured, representing the morphing flap. Using a density of  $1.184 \text{ kg/m}^3$ , dynamic viscosity of  $1.983 \times 10^{-5} \text{ kg/m.s}$ , chord length of  $2 \text{ m}$ , and velocity of  $50 \text{ m/s}$ , the Reynolds number was calculated as approximately  $6,000,000$ . Using this in the viscous analysis and an angle of attack of  $5^\circ$ , the resultant forces and moment acting at the flap “hinge” were found as:  $F_{HX} = 214.86 \text{ N/m (span)}$ ,  $F_{HY} = 778.43 \text{ N/m (span)}$  and  $M_H = 155.11 \text{ Nm/m (span)}$ . When considering a span of  $0.1 \text{ m}$ , the major  $F_{HY}$  load is  $77.84 \text{ N (} 7.93 \text{ kg}_f)$ . This is considerably smaller than the load used in the finite element analysis ( $50 \text{ kg}_f$ ) which suggests

the feasibility of the morphing design. As the skin was not included in the modeling, the magnitude of this force was distributed evenly across the top surface of the vertical junctions of the structure.

The results of the three load cases are shown in Fig. 10 and Table 1. From Fig. 10 (a) it is clear that the desired morphing profile is achieved. The deflection  $\delta$  of  $8.06^\circ$  was achieved for a no air-load case at the input pressure and the deflection was  $-10.15^\circ$  for a no pressure-input case at the given air load. The deflection for the combined load case was  $0.42^\circ$  showing that the pressure can be used to control both the deflection and stiffness of the structure. The maximum stress and strain values occurred at the junction between the top and lower arches for each cell. The high values of stress are due to the single nodal connection point (for each point along the span) between these two arches. The stress level can be reduced by using a more

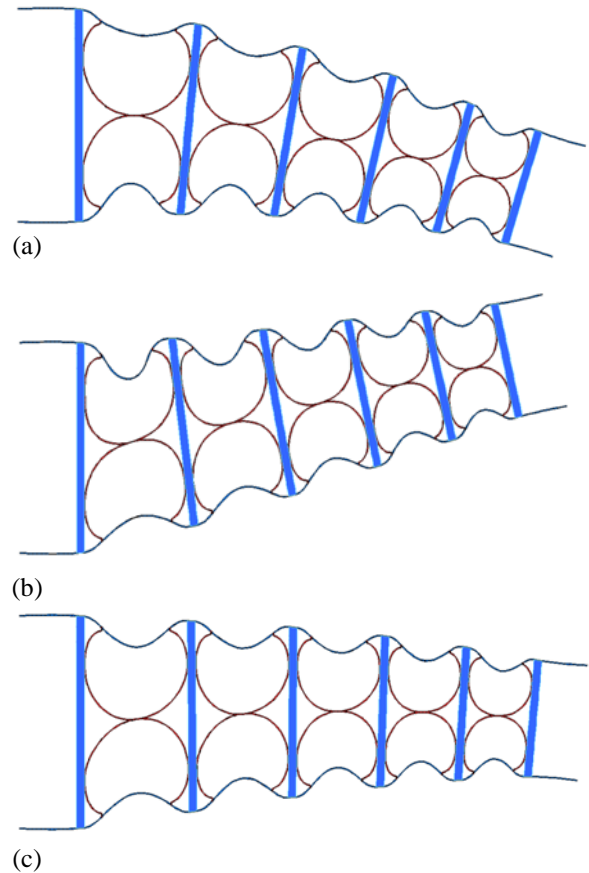


Fig. 10 Deformation results of finite element analysis. (a) Pressure case; (b) force case and (c) combined pressure-force case.

gradual connection between the two arches. The maximum strain was in the order of 2 per cent.

	P	F	P + F
$\delta$ , deg	8.06	-10.15	0.42
$\sigma_{vm\ max}$ , MPa	797	637	432
$\epsilon_{vm\ max}$	0.0203	0.0165	0.0101

**Table 1** Deflection, stress and strain finite element analysis results.

### 5.3 Fabrication and Testing

A specimen of the same geometry as above was fabricated using glass fiber reinforced plastic (GFRP). The specimen measured 340 (chord)  $\times$  350 mm (span). In order to achieve the correct geometry of the cellular morphing structure, two foam molds were cut using a CNC hot wire cutter. The molds were separated into: i) a continuous connection of the lower arches and ii) a continuous connection of the upper arches. The mold surfaces were first hardened by applying epoxy resin and then coated with wax and mold release poly vinyl alcohol (PVA) as per the usual wet lay-up procedure. As the structure is symmetric about the horizontal  $X_0$  axis, two specimens were made for each mold and then bonded together in a mirrored manner using another foam mold as a “jig” to keep the components in place. The vertical inserts and the trailing edge tip were fabricated from a GFRP-foam sandwich-type structure. The pressure was enforced on the surfaces by using bladders manufactured from 0.4 mm thick neoprene rubber. The bladders were pressurized using one electronic pressure controller for cell 1, a second controller for cells 2 and 3 (split using a pneumatic manifold) and a third controller for cells 4 and 5. This arrangement was chosen as cell 1 has the largest volume and required independent pressure control. It should be noted that only one row of cells (top or bottom) was controlled at a time. To swap the pressurization of the rows, the pneumatic tubes were disconnected from one set of cells and connected to the other set. The experimental setup is shown in Fig. 11. Fig. 12 shows the structure with and without the bladders inserted.

The preliminary results of the testing of this first-version prototype are given in Fig. 13

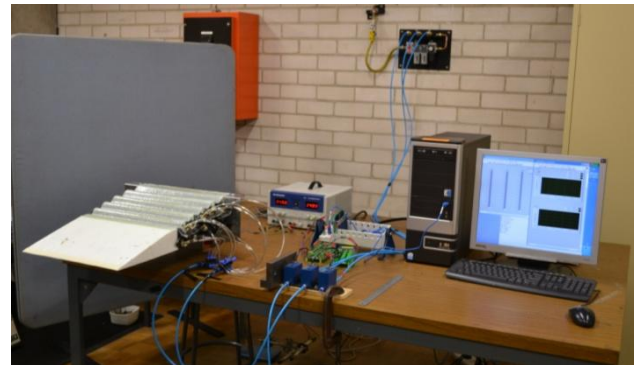


**Fig. 11** Experimental setup.

and Fig. 14. In these figures, “Stage” refers to the pressure input: stage 1 is cell 1 pressurized, stage 2 is cells 1 to 3 pressurized and stage 3 is all five cells pressurized. The maximum pressure used for testing was 14 kPa and the structure was tested through pressurization and depressurization sequentially. Fig. 13 shows that the desired morphing profile is achieved and that bimorph type shape change can be achieved. The maximum x-displacements (in either direction) were -35 mm and 4 mm for top and bottom pressurization respectively. The maximum y-displacements were -127 mm and 43 mm for top and bottom pressurization respectively. It should be noted for the graphs in Fig. 14 that the path during pressurization and depressurization was identical for the pressurization of the bottom cells and the

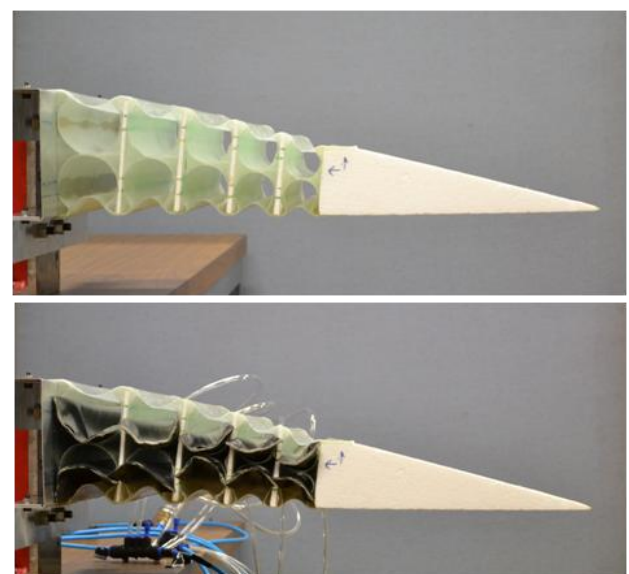


**Fig. 12** (a) Structure without bladders. (b) Structure with bladders and pneumatic tubing.

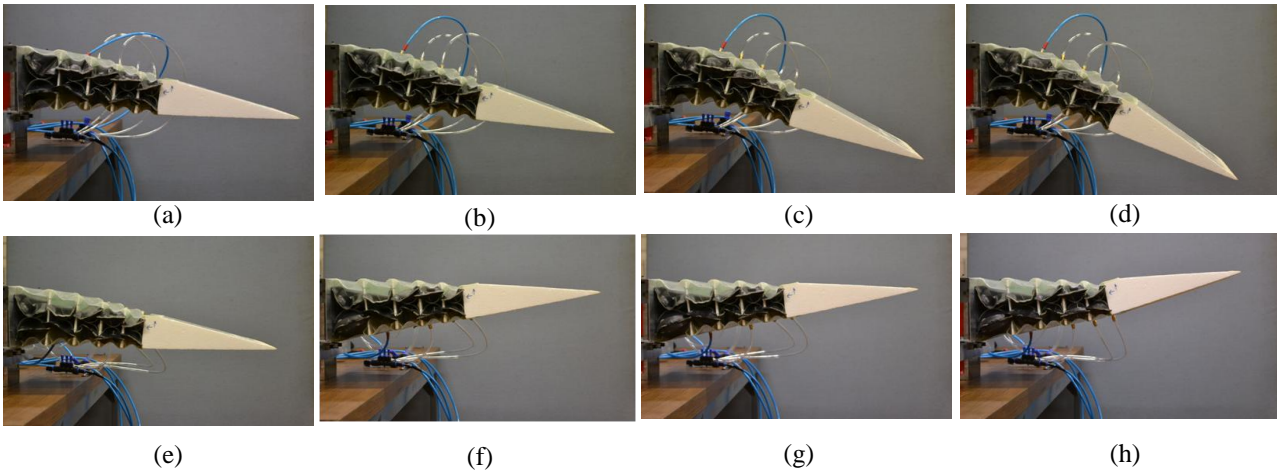


**Fig. 13** (a) – (d) Top cells pressurized for stages 0 to 3 respectively resulting in downward tip deflection. (e) – (h) Bottom cells pressurized for stages 0 to 3 respectively resulting in upward tip deflection.

direction of pressurization is given by the arrow for the pressurization of the top cells. The accumulation of the displacement is evident across the cells as the displacement increases with increasing stage. The angular deflection was obtained using Eqn 4 where  $L_f$  is the length of the flap (550 mm). The maximum downward flap deflection was  $13.9^\circ$  and the maximum upward deflection was  $4.4^\circ$ . This lower upward deflection was caused by the influence of gravity.

$$\delta = \tan^{-1}\left(\frac{DY}{L_f + DX}\right) \quad (4)$$

### 7 Concluding Remarks

In this work, it was shown that a morphing trailing edge control surface can be achieved through modification of a 2D topology optimization result. The finite element analysis and testing results demonstrate the working concept and feasibility of the design. Future work includes manufacturing and testing of a second-version prototype including the skin components and the consideration of alternate 3D cellular morphing strategies.

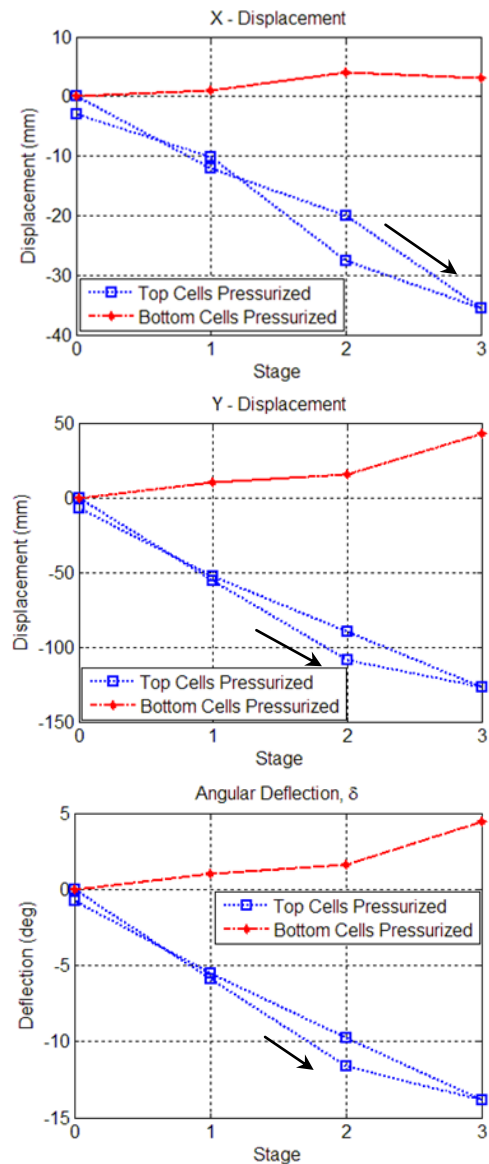


**Fig. 14** (a) X and (b) Y displacements of the tip and (c) angular deflection.

## Acknowledgements

Srinivas Vasista is a recipient of the Australian Postgraduate Award and the R.W. McKenzie Scholarship for Aeronautical Sciences and Technology and is grateful for the support from the Commonwealth Government of Australia and the R.W. McKenzie Centre. The authors would like to thank the support of the Australian Research Council (Grant No. DP110104123). The authors would also like to thank Matthew Anderson for providing extensive assistance during the manufacturing process of the test specimen.

## References

- [1] Thill C, Etches J, Bond I, Potter K and Weaver P. Morphing skins. *The Aeronautical Journal*, Vol. 112, No. 3, pp. 117-138, 2008.
- [2] Stanewsky E. Aerodynamic benefits of adaptive wing technology. *Aerospace Science and Technology*, Vol. 2000, No. 4, pp. 439-452, 2000.
- [3] Vasista S, Tong L and Wong K C. Realization of morphing wings - a multidisciplinary challenge. *Journal of Aircraft*, Vol. 49, No. 1, pp. 11-28, 2012.
- [4] Sundaresan V B and Leo D J. Chemo-mechanical model for actuation based on biological membranes. *Journal of Intelligent Material Systems and Structures*, Vol. 17, No. 10, pp. 863-870, 2006.
- [5] Shan Y, Philen M, Bakis C E, Wang K W and Rahn C D. Nonlinear-elastic finite axisymmetric deformation of flexible matrix composite membranes under internal pressure and axial force. *Composites Science and Technology*, Vol. 66, No. 15 pp. 3053-3063, 2006.
- [6] Kirn J, Lorkowski T and Baier H. Development of flexible matrix composites (FMCs) for fluidic actuators in morphing systems. *International Journal of Structural Integrity*, Vol. 2, No. 4, pp. 458-473, 2011.
- [7] Shan Y, Philen M, Lotfi A, Suyi Li, Bakis C E, Rahn C D and Wang K W. Variable stiffness structures utilizing fluidic flexible matrix composites. *Journal of Intelligent Material Systems and Structures*, Vol. 20, No. 4, pp. 443-456, 2009.
- [8] Vos R and Barrett R M. Pressure Adaptive Honeycomb: A novel concept for morphing aircraft structures. *27th International Congress of the Aeronautical Sciences*, Nice, France, 2010.
- [9] Vos R, Barrett R and Romkes A. Mechanics of Pressure-Adaptive Honeycomb. *Journal of Intelligent Material Systems and Structures*, Vol. 22, No. 10, pp. 1041-1055, 2011.
- [10] Vasista S and Tong L. Design and testing of pressurized cellular planar morphing structures. *AIAA Journal*, Vol. 50, No. 6, pp. 1328-1338, 2012.
- [11] Vasista S and Tong L. Pressurized morphing wing structures. *53rd Structures, Structural Dynamics, and Materials Conference*, Hawaii, United States, AIAA-2012-1905, 2012.
- [12] Tong L and Lin J. Structural topology optimization with implicit design variable - optimality and algorithm. *Finite Elements in Analysis and Design*, Vol. 47, No. 8, pp. 922-932, 2011.
- [13] Sigmund O and Clausen P M. Topology optimization using a mixed formulation: An alternative way to solve pressure load problems. *Computer Methods in Applied Mechanics and Engineering*, Vol. 196, No. 13-16, pp. 1874-1889, 2007.
- [14] Zienkiewicz O C and Taylor R L. *The finite element method*. Butterworth Heinemann, 2000.
- [15] Drela M and Youngren H, XFOIL, software package ver. 6.9, 2001

## Copyright Statement

The authors confirm that they, and/or their company or organization, hold copyright on all of the original material included in this paper. The authors also confirm that they have obtained permission, from the copyright holder of any third party material included in this paper, to publish it as part of their paper. The authors confirm that they give permission, or have obtained permission from the copyright holder of this paper, for the publication and distribution of this paper as part of the ICAS2012 proceedings or as individual off-prints from the proceedings.